REPORT DOCUMENTATION PAGE

Form Approved
OMB No. 0704-0188

1. REPORT DATE *(DD-MM-YYYY)*	2. REPORT TYPE	3. DATES COVERED *(From - To)*
03/11/2020	Final Technical	01/10/2020 - 31/01/2020

4. TITLE AND SUBTITLE

Modeling of Induction Infrared Thermography for Non-Destructive Evaluation of Alloy Sensitization

5a. CONTRACT NUMBER

5b. GRANT NUMBER

N00014-18-1-2059

5c. PROGRAM ELEMENT NUMBER

6. AUTHOR(S)

Matthew Roberts
Emily Guzas
Keving Wange (Virginia Tech PI)

5d. PROJECT NUMBER

5e. TASK NUMBER

5f. WORK UNIT NUMBER

7. PERFORMING ORGANIZATION NAME(S) AND ADDRESS(ES)

Virginia Polytechnic Institute and State University
Office of Sponsored Programs
North End Center
300 Turner Street NW, Suite 4200
Blacksburg, VA 24061-0001

8. PERFORMING ORGANIZATION REPORT NUMBER

9. SPONSORING/MONITORING AGENCY NAME(S) AND ADDRESS(ES)

ONR REG Office Atlanta
100 Alabama Street, SW Suite 4R15
Atlanta, GA 30303

10. SPONSOR/MONITOR'S ACRONYM(S)

ONR

11. SPONSOR/MONITOR'S REPORT NUMBER(S)

12. DISTRIBUTION/AVAILABILITY STATEMENT

Distribution A

13. SUPPLEMENTARY NOTES

None

14. ABSTRACT

This project investigates the efficacy of using induction infrared thermography (IIRT) as a non-destructive method for detecting welding-induced sensitization in stainless steels, using a combined experimental and computational approach. A series of laboratory experiments have been conducted to demonstrate this method, using a radio frequency function generator, an induction wand, a FLIR SC8203 infrared camera, and the 440C steel as a representative material. Traditional metallography techniques and scanning electron microscopy (SEM) have been employed to identify the location of any sensitized regions and characterize the corresponding microstructure. For welded 440C steel plates, the IIRT experimental results reveal a distinguishable heat signature, with higher temperature observed within the sensitized regions. Next, a computational study has been conducted to simulate the IIRT experiment and investigate the underlying physics. A three-dimensional thermo-electro-magnetic model has been adopted, which combines Fourier's law of heat conduction and Maxwell's equations for predicting the electromagnetic field caused by a sinusoidal excitation current flowing through the induction coil. We solve the system of governing equations using the commercial solver COMSOL Multiphysics. To numerically investigate the possible causes of the disproportionate heating within the sensitized regions, the values of electrical resistivity and magnetic permeability therein are varied. The simulated results indicate that the heat signature observed in the laboratory experiment may result from the increase of both electrical resistivity and magnetic permeability in the HAZ.

15. SUBJECT TERMS

Induction infrared thermography; Eddy current thermography; Sensitization; Corrosion; Stainless steel; Numerical simulation; Non-destructive testing and evaluation

16. SECURITY CLASSIFICATION OF:			17. LIMITATION OF ABSTRACT	18. NUMBER OF PAGES	19a. NAME OF RESPONSIBLE PERSON
a. REPORT	b. ABSTRACT	c. THIS PAGE			Dr. Kevin Wang
U	U	U	Unclassified Unlimited distribution	23	19b. TELEPHONE NUMBER *(Include area code)* 540-231-6611

Modeling of Induction Infrared Thermography for Non-Destructive Evaluation of Alloy Sensitization

- Final Report -

Award Number: N00014-18-1-2059

Matthew Roberts[1] Emily Guzas[2] Kevin Wang[1]

[1]Department of Aerospace and Ocean Engineering, Virginia Polytechnic Institute and State University
Blacksburg, VA 24061
[2]Naval Undersea Warfare Center, Division Newport Newport, RI 02841

August 7, 2020

Abstract

This project investigates the efficacy of using induction infrared thermography (IIRT) as a non-destructive method for detecting welding-induced sensitization in stainless steels, using a combined experimental and computational approach. A series of laboratory experiment have been conducted to demonstrate this method, using a radio frequency function generator, an induction wand, a FLIR SC8203 infrared camera, and the 440C steel as a representative material. Traditional metallography techniques and scanning electron microscopy (SEM) have been employed to identify the location of any sensitized regions and characterize the corresponding microstructure. For welded 440C steel plates, the IIRT experimental results reveal a distinguishable heat signature, with higher temperature observed within the sensitized regions. Next, a computational study has been conducted to simulate the IIRT experiment and investigate the underlying physics. A three-dimensional thermo-electro-magnetic model has been adopted, which combines Fourier's law of heat conduction and Maxwell's equations for predicting the electromagnetic field caused by a sinusoidal excitation current flowing through the induction coil. We solve the system of governing equations using the commercial solver COMSOL Multiphysics. To numerically investigate the possible causes of the disproportionate heating within the sensitized regions, the values of electrical resistivity and magnetic permeability therein are varied. The simulated results indicate that the heat signature observed in the laboratory experiment may result from the increase of both electrical resistivity and magnetic permeability in the HAZ.

1 Distribution Statement

2 Background

Sensitization is a well-known issue that affects the corrosion resistance of many alloys used in naval applications, including stainless steels, aluminum alloys, and nickel alloys. It refers to the formation of certain chemical compounds — for example, chromium carbide ($Cr_{23}C_6$) in stainless steels and β-phase magnesium aluminide (Al_3Mg_2) in aluminum-magnesium alloys — due to elevated temperature [1, 2, 3, 4, 5]. The

precipitation of these compounds at grain boundaries makes the alloy susceptible to intergranular corrosion (IGC), environmentally-assisted cracking (EAC), and broader fracture. In particular, for many stainless steels (e.g., the AISI 300 and 400 series), sensitization occurs after a sample or component has its temperature raised above a critical threshold (in excess of 600 ℃) for a certain length of time, followed by a cooling period [1, 6, 7]. With chromium being a primary contributor to a stainless steel's corrosion-inhibiting properties, the formation of chromium carbide depletes the grain boundaries of these benefits. In practice, welding is often the primary cause of sensitization in medium- and high-carbon stainless steels. During welding, temperatures in the heat-affected zones (HAZ) adjacent to a weld may reach 600-900 ℃ [8]. Following published phase diagrams for carbide precipitation, this means that welding introduces enough heat within the HAZ to initiate the formation of chromium carbide in as soon as 50 seconds [7, 9].

Current methods for sensitization detection require chemical and/or microscopic imaging tests of small material samples in a carefully controlled laboratory environment (e.g., [10, 11, 12, 13, 14, 15, 16]). These methods are usually destructive in nature and can be time-consuming. For example, the ASTM standard procedures A262, Practices B, C, and F (for certain types of steels) and G67 (for certain types of aluminum alloys) require immersing small material samples in a strong acid for at least one day, after which the resulting mass loss is measured to draw conclusions on the extent of sensitization [10, 11]. Despite their effectiveness for detecting sensitization, it is not practical to use these methods to inspect materials and structures that are already in production or service. Thus, a non-destructive, *in situ*, fast method for sensitization detection is clearly desirable.

Several non-destructive testing and evaluation methods for sensitization detection have been investigated in the past. For example, Shaikh *et al.* applied the eddy current testing (ECT) method to correlate eddy current amplitudes to the degree of sensitization (DOS), both in aged samples and in samples that had previously undergone the ASTM A262 Strauss test [17]. Kikuchi *et al.* have explored a technique to detect sensitization in samples using a Hall sensor, measuring differences in magnetic properties due to the presence of sensitization [18]. Abraham *et al.* investigated the use of nonlinear ultrasonics (NLU), and drew a correlation between the ASTM test result of the DOS and the ratio of the first and second harmonic amplitudes [19]. Also, Cobb *et al.* used electromagnetic acoustic transducer (EMAT) ultrasound to examine aluminum specimens, correlating velocity ratios to the DOS [20]. Furthermore, Stella *et al.* showed that a difference in low and high levels of sensitization could be qualitatively resolved through differences in their ultrasonic attenuation and power spectra [21]. Despite many encouraging results, the methods presented in these studies also have some limitations. For example, the method of ECT is generally not practical for the scanning of large or complex geometries, an impediment to detecting sensitization as it is not always present in small or obvious locations. Also, Cobb *et al.* showed that EMAT ultrasound can clearly identify high DOS in a 5000-series aluminum alloy, but is less effective for samples of the same alloy with low or medium DOS [20].

Induction infrared thermography (IIRT) has been used as a non-destructive, non-intrusive method for detecting defects and cracks in conducting materials, particularly metals. Also known as eddy current infrared thermography, IIRT works by sending an AC current through a conductive metal coil to generate a time-varying electromagnetic field near the coil. When this field is near a metal surface, it will electrically couple to that surface and induce eddy currents in the metal. The depth of penetration can be characterized using the skin depth, δ, defined as the depth at which the density of eddy currents drops to $1/e$ (≈ 0.368) times that at the surface. Specifically,

$$\delta = \sqrt{\frac{2}{\omega\mu\sigma}}, \tag{1.1}$$

where μ and σ denote the magnetic permeability and electrical conductivity (reciprocal of electrical resistivity) of the material, respectively. ω is the angular frequency in the coil. As a method of non-destructive evaluation and testing, IIRT is based on the premise that eddy currents are induced within the specimen in a flow pattern dictated by the direction and magnitude of the coil's electromagnetic field, where the flow would be disturbed by any discontinuity in geometry (e.g., flaws such as cracks or voids) or material properties [22, 23, 24, 25, 26, 27]. Near such discontinuities, the eddy currents are forced to take alternate

paths that generate differing heat signatures when compared to what would have been witnessed in the same material, but in the absence of any abnormalities. Areas with altered paths can then be examined with an infrared camera and analyzed/characterized to make predictions on the location, shape, and size of the abnormality. For example, Oswald-Tranta performed IIRT experiments on steel samples showing that IIRT could detect disturbances in eddy current flow in the vicinity of surface cracks extending 1 mm deep into their samples [26, 28]. The experiments, and developed finite element models of the IIRT experiments, showed the differences in the induced eddy currents in the vicinity of a 1 mm deep surface crack, as a function of skin depth (0.1 mm or 1.0 mm for their steel samples). The use of infrared imaging allows IIRT to be used for *in situ*, full-field measurement.

Recently, Tucker *et al.* investigated the feasibility of using IIRT to detect sensitization in stainless steels [9]. They demonstrated that after a few seconds of induction heating, the sensitized region can produce a distinguishable heat signature under an infrared camera. Nonetheless, the physical mechanism responsible for this result is still unclear. It has been hypothesized that because of the precipitation of chromium carbide, the sensitized grain boundaries have a higher electrical resistivity than the original, non-sensitized grain structure. Therefore, under electromagnetic induction, more resistive heat is generated within the sensitized region. So far, the validity of this hypothesis has not been investigated in detail. In particular, it is unclear if the variation of electrical resistivity within sensitized grain boundaries is the primary reason for the distinguishable heat signature. Therefore, a quantitative physical model that can explain the observed IIRT result is desirable.

3 Major goals and objectives of the project

This project aims to investigate efficacy of using IIRT as a non-destructive method for detecting welding-induced sensitization in stainless steels. The technical objectives of the project are the following.

- Develop a multiphysics (thermo-electro-magnetic) computational model capable of predicting the IIRT heat signatures of sensitized chromium steels.
- Quantitatively validate the computational model by conducting IIRT experiments and standard destructive sensitization tests.
- Elucidate the correlation between the IIRT heat signature and sensitization status for welded 440C stainless steel samples.

4 Accomplishments

We have conducted a combined experimental and computational study to demonstrate and assess the IIRT approach in the context of detecting welding-induced sensitization in AISI 440C steel specimens. The 440C steel has a high carbon content of $0.95 - 1.20$ wt% and a chromium content of $16 - 18\%$; therefore it is prone to sensitization during welding and heat treatments.

We start with presenting our experimental study to demonstrate the feasibility of the method, using a hairpin-shaped copper induction wand and a FLIR SC8203 infrared camera. We applied traditional metallography techniques and scanning electron microscopy (SEM) to identify the location of sensitized material and characterize the corresponding microstructure. Next, we present our computational study to simulate the IIRT experiment and compare with the experimental data. Specifically, a thermo-electro-magnetic model is adopted, which includes Fourier's law of heat conduction and Maxwell's equations for predicting the electromagnetic field caused by a sinusoidal excitation current through the induction coil. Additionally, we introduced an empirical model to relate the density and thickness of sensitized grain boundaries with the local increase in eddy current density that is solved using the commercial solver COMSOL Multiphysics [29].

4.1 Specimen preparation and inspection

Sensitized 440C steel samples are prepared by welding two rectangular plates of thickness 3.2 mm (0.125 in) together using an off-the-shelf 309 filler rod. The 309 material is an austenitic chromium-nickel with a carbon content of 0.2 wt%. The weld bead has a width of 6.35 mm (0.25 in). The combined plate has a length of 220 mm (8.66 in) along the weld line and a width of 303 mm (11.9 in) transverse to the weld line. No further surface treatments are applied. Figure 1(a) shows one sample after welding. The high welding temperature and relatively slow cooling is expected to sensitize the steel within the heat affected zones on both sides of the weld (Figure 1(b)).

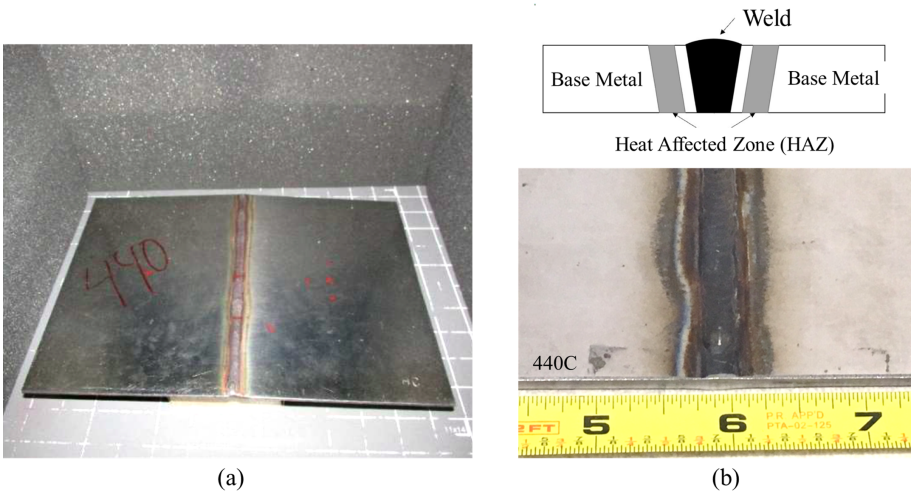

Figure 1: A welded AISI 440C steel plate for evaluating the method of using IIRT for non-destructive sensitization detection. (a) A photo of the entire welded plate. (b) A schematic drawing of a cross section through the weld line, and a close-up photo.

Although the HAZ can be seen by the naked eye, the sensitization status (i.e. sensitized or not) of the sample cannot be determined by visual inspection. Therefore, we use traditional metallography techniques and SEM to confirm the presence of sensitization within the HAZ. Specifically, 25.4 mm $\times$ 6.35 mm (1 in $\times$ 0.25 in) samples are cut transverse to the weld. Each sample includes the weld, and the HAZ and the base metal to either side of the weld. The samples are mounted in cylindrical pucks of epoxy resin, with metal screws in contact with the embedded face of the samples and protruding from the back side of the epoxy (Figure 2). The sample surface is polished to 0.01 μm surface roughness, following ASTM A262-15 and ASTM E3-11(2017) [30]. After polishing, electrolytic etching with 10% oxalic acid (by weight) is introduced to the sample, following ASTM A763-15, Procedure W [31] and ASTM A262-15, Practice A.

Figure 3 presents an SEM image taken within one HAZ of the specimen shown in Fig. 2, in comparison with another one taken within the base material. As expected, the grain boundaries within the HAZ exhibit significant corrosion from the applied etchant. This indicates the formation and precipitation of chromium carbide at the grain boundaries within this particular region, which is the main characteristic of sensitization in stainless steels.

4.2 Induction infrared thermography (IIRT) experiment

Figure 4 shows the setup of the IIRT experiment. In particular, the IIRT experiments make use of the Induction Thermography System (ITS) manufactured by Qi2. The ITS 100 system includes a radio frequency

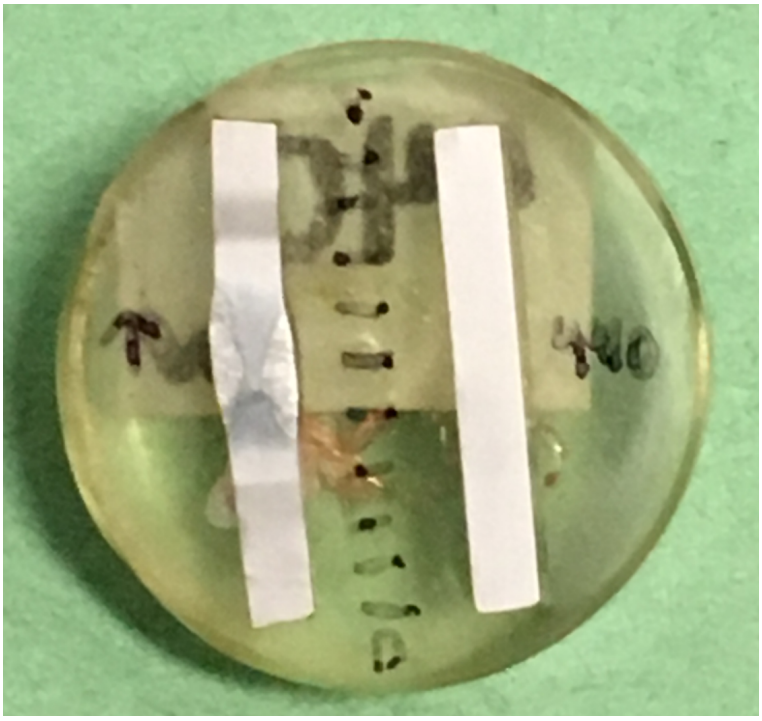

Figure 2: Mounted specimens for SEM measurement. Left: A sample that includes the weld, the HAZ, and the base material. Right: Base material.

(RF) power unit, a personal computer data acquisition system (PCDAS), and an externally triggered induction wand unit. While the induction wand unit includes interchangeable coils in various configurations, a hairpin-shaped copper coil is used in the experiments to obtain an easy-to-process heating pattern. The coil has a circular cross-section, with a diameter of 6.35 mm (0.25 in). The straight portions of the coil are over 305 mm (12 in) long and are separated by a center-to-center distance of 50.8 mm (2 in). Figure 4(a) shows the FLIR 8203 infrared camera atop the view guide and pointed down at the specimen below it.

The bottom of the camera view guide is placed 397 mm (15.63 in) above the table top surface. The testing area is surrounded by 51 mm (2 in) thick foam insulation panels on three sides, to isolate the experiment from undesirable incidental heat and light sources. Two small ($85.7 \times 57.2 \times 34.9$ mm) cardboard boxes are used to support the specimen aloft 34.9 mm (1.37 in) above the table surface and decouple it from any incidental heating from the table.

The main steps of the IIRT experiment can be summarized as follows.

(1) The plate specimen is placed on the cardboard boxes underneath the camera.

(2) The FLIR infrared camera is brought into focus on the sample top surface to ensure that the images and data collected is as finely resolved as possible.

(3) A background thermal scan is performed in conjunction with a temperature reading with a handheld infrared thermometer to relate the intensity value measured by the camera to the baseline conditions for that sample within the laboratory.

(4) The induction coil is covered in a fine, thin nylon netting, which is placed in contact with the specimen under inspection and energized with the external power supply. The coil liftoff distance is effectively 1.6 mm (0.06 in) from the sample surface due to the presence of a nylon netting on the coil.

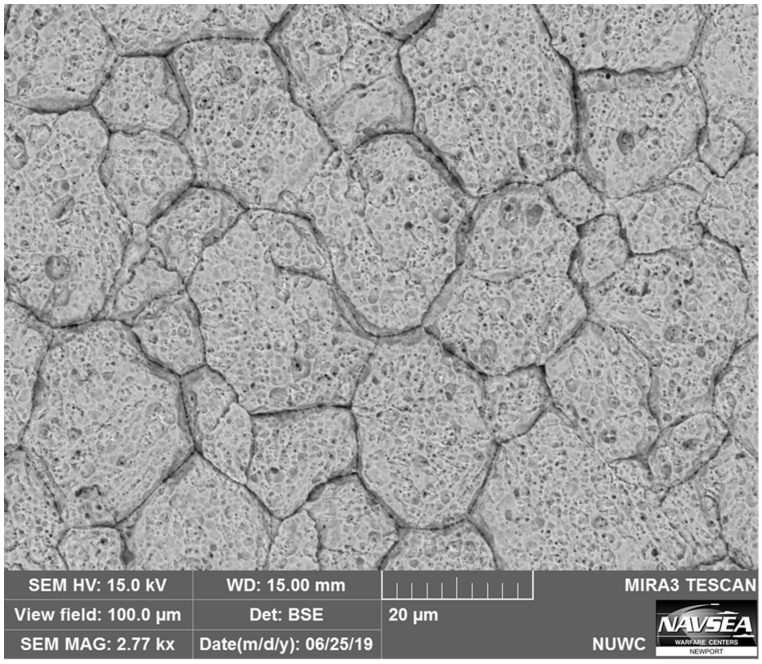

(a)

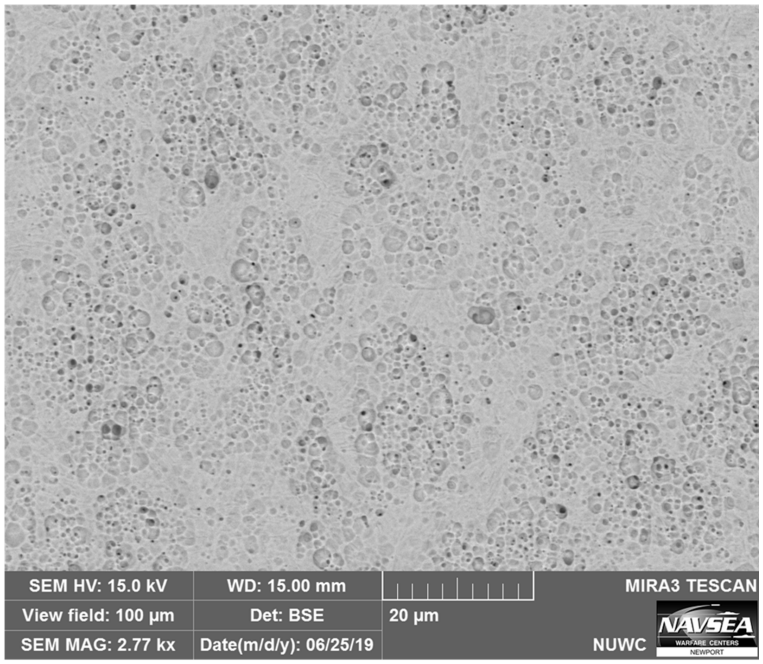

(b)

Figure 3: Scanning electron microscopy (SEM) images at two different locations. (a) At the middle of a HAZ (sensitized). (b) Within the base material (unsensitized).

(5) The excitation is performed for a designated period (usually between 2 s and 3 s) with the induction wand held in a fixed location. After completion of the excitation period, the wand is held in place with the IR camera continuing to record data until the capture period completes (usually a total of 10 s, inclusive of wand heating time).

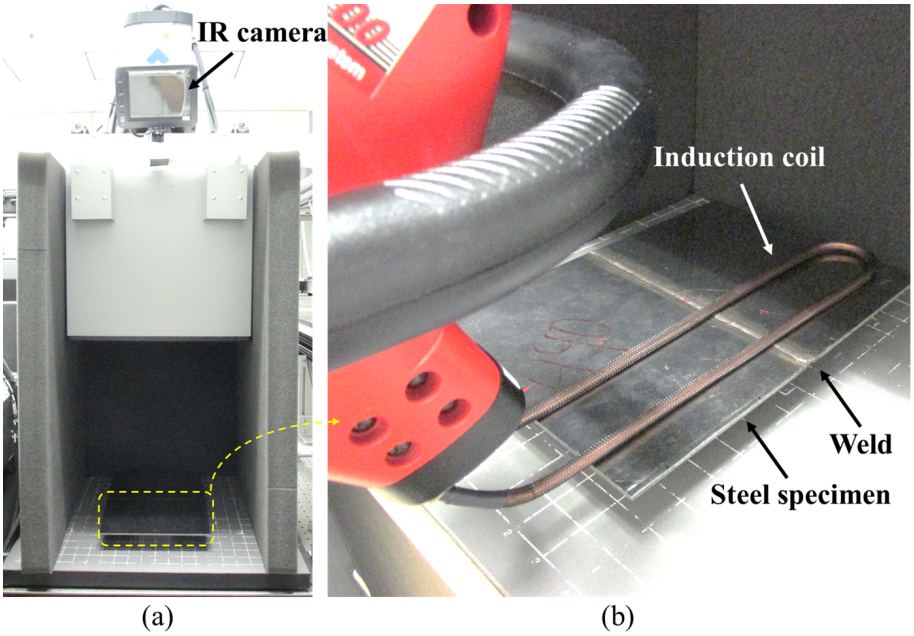

Figure 4: Setup of the induction infrared thermography (IIRT) experiment for sensitization detection.

There are several differences between the IIRT experimental procedure discussed herein and prior IIRT experiments by the authors [9]. First, the induction wand is held stationary for the duration of the data capture. In the prior experiments [9], the wand was swept at a moderate pace (about 72 mm/s) across the sample surface by the operator. Second, we calibrated the recorded intensity counts to measured temperatures in order to convert experimental results into more meaningful physical quantities, and to also provide a head-to-head comparison to simulated results.

The key processes underlying the above IIRT experiment include electromagnetic induction within the welded plate specimen, the generation of heat from the induced eddy currents, and the diffusion of heat. Specifically, by placing the induction coil near the (conductive) plate specimen and passing an alternating current through the coil at a prescribed frequency, a rapidly varying magnetic field is created that penetrates the specimen and induces eddy currents near its surface [25, 32]. The induced currents flowing within the specimen will generate heat through Joule heating. The rate of heat generation depends on both the electrical resistivity of the material and the eddy current density. The spatial and temporal variation of temperature is then captured by the infrared camera. In particular, differences between a sensitized region and an unsensitized region in magnetic resistivity or electrical conductivity should lead to distinct heat signatures in the infrared thermal images.

4.3 Modeling and simulation

The primary equations governing induction originate from the magnetic vector potential formulation of the electromagnetic diffusion equation derived from Maxwell's equations. The frequency of the induction source for the described IIRT experiments is of the order of 10^5 Hz. In comparison, the time scale of the IIRT

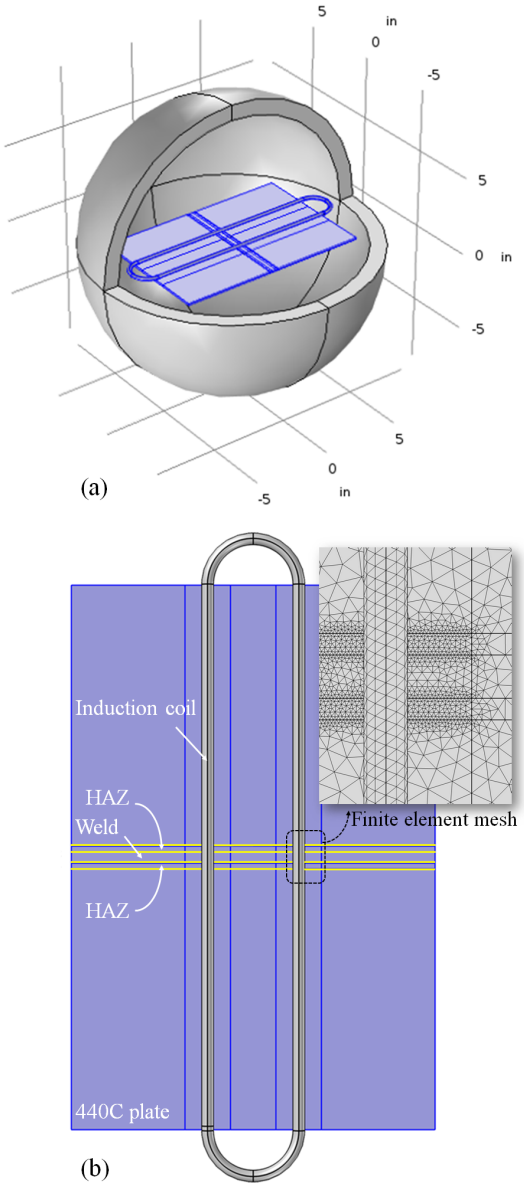

Figure 5: The COMSOL Multiphysics simulation model. (a) A perspective view of the 3D computational domain, with the subdomain of the air removed for visibility. (b) A top view of the induction coil and the steel specimen.

experiment is of the order of seconds. The disparity of time scales between the variation of current in the induction wand and the IIRT experiment justifies the solution of the electromagnetic equation in frequency domain. Specifically,

$$i\omega\sigma\mathbf{A} - \frac{1}{\mu}\nabla^2\mathbf{A} = \mathbf{J}_s, \tag{1.2}$$

where i is the imaginary unit. $\mathbf{A}$ denotes the magnetic vector potential, $\mathbf{J}_s$ the current density of the induction source, and ω the angular frequency of the current. μ and σ denotes magnetic permeability and

Specimen (440C Steel Plate)			
Thickness (mm)	3.175	Length (m)	0.305
Width (m)	0.2032	Mass Density, ρ (kg/m^3)	7,700
Rel. Magnetic Permeability, μ_r	700	Rel. Permittivity, ε_r	1.0
Electrical Conductivity, σ (S/m)	1.69×10^6	Thermal Conductivity, k (W/(m K))	24.2
Specific Heat, c_p (J/(kg K))	450		
Specimen Weld (309 Filler)			
Thickness (mm)	3.175	Length (m)	0.2032
Width (mm)	6.35	Mass Density, ρ (kg/m^3)	8,000
Rel. Magnetic Permeability, μ_r	500	Rel. Permittivity, ε_r	1.0
Electrical Conductivity, σ (S/m)	1.28×10^6	Thermal Conductivity, k (W/(m K))	15.6
Specific Heat, c_p (J/(kg K))	500		
Induction Coil (Copper)			
Hairpin Radius (mm)	3.175	Length (m)	0.31
Current (A)	19	Mass Density, ρ (kg/m^3)	8,960
Rel. Magnetic Permeability, μ_r	1.0	Rel. Permittivity, ε_r	1.0
Electrical Conductivity, σ (S/m)	5.998×10^7	Thermal Conductivity, k (W/(m K))	400
Specific Heat, c_p (J/(kg K))	385	Frequency of AC Current, f (kHz)	245
Air			
Mass Density, ρ (kg/m^3)	1.2	Rel. Magnetic Permeability, μ_r	1.0
Rel. Permittivity, ε_r	1.0	Electrical Conductivity, σ (S/m)	1.0
Thermal Conductivity, k (W/(m K))	0.026	Specific Heat, c_p (J/(kg K))	1000

Table 1: Geometry and material parameters used in the simulations

electrical conductivity, respectively. More specifically,

$$\mu = \mu_0 \mu_r, \tag{1.3}$$

where $\mu_0 = 4\pi \times 10^{-7}$ H/m is the permeability of free space, and μ_r is the relative magnetic permeability of a material. For the modeled IIRT experiment, both μ and σ can be treated as constant properties within a given material. Additional details on the derivation of Eq. (1.2) are provided in the Appendix.

Once the eddy currents are induced within a sample, the resultant bulk heating generated by induction is represented by

$$q_{ind} = \frac{1}{\sigma}|\mathbf{J}|^2, \tag{1.4}$$

where

$$\mathbf{J} = -i\omega\sigma\mathbf{A} \tag{1.5}$$

is the induced eddy current density. The induced heat is then used as the source term in Fourier's law of heat conduction to describe the conduction through the specimen, i.e.

$$\rho c_p \frac{\partial T}{\partial t} - \nabla \cdot (k \nabla T) = q_{ind} - q_{conv} - q_{rad}. \tag{1.6}$$

Here, ρ is the mass density of the material, T is the temperature, k the thermal conductivity, and c_p the specific heat. q_{conv} and q_{rad} represent, respectively, the heat losses due to convection and radiation, given by

$$q_{conv} = h(T - T_\infty) \tag{1.7}$$

and

$$q_{rad} = \epsilon \sigma_s (T^4 - T_\infty^4), \tag{1.8}$$

where T_∞ denotes the ambient temperature, h the convective heat transfer coefficient, ϵ the dimensionless emissivity for a given material, and $\sigma_s = 5.6703 \times 10^8$ W/(m^2 K^4) the Stefan-Boltzmann constant.

The equation for the heat conduction is solved in the time domain to find the temperature at a given time and location in the specimen. COMSOL Multiphysics 5.3a and its AC/DC Module [29] are employed to create and numerically solve the induction heating problem.

Figure 5 presents the simulation model, which includes the sample plate, a hairpin-shaped induction coil, and the surrounding air. The geometry and material properties are specified based on the experiment setup (Table 1).

The thickness of the plate is exactly matched to that in the experiments, i.e. $t = 3.2$ mm (0.125 in). The length and width are approximated. As the critical heating of the plate occurs in a region sufficiently far from the plate edges (in the middle, underneath the coil), it is unnecessary to explicitly model the outermost plate edges.

For the 440C steel and the induction unit used, the skin depth, δ, is 0.00317 mm, which is three orders of magnitude lower than the thickness of the specimen. Therefore, we can assume that for both the specimen and the induction coil, all the induced eddy currents are concentrated near the surface. Given this assumption, we can apply the following impedance boundary condition (also known as Leontovich boundary condition) [33, 34] at the surface of the specimen and the induction coil:

$$\sqrt{\frac{\mu}{\varepsilon - \frac{i\sigma}{\omega}}}\mathbf{n} \times \mathbf{H} + \mathbf{E}_i - (\mathbf{n} \cdot \mathbf{E}_i)\mathbf{n} = (\mathbf{n} \cdot \mathbf{E}_s)\mathbf{n} - \mathbf{E}_s, \tag{1.9}$$

where $\mathbf{n}$ denotes the unit normal of the boundary and ε is the material's permittivity. Specifically,

$$\varepsilon = \varepsilon_0 \varepsilon_r, \tag{1.10}$$

where ε_0 denotes the vacuum permittivity, and ε_r the material's relative permittivity. $\mathbf{E}_i$ and $\mathbf{E}_s$ denote the induced electric field and applied (i.e. source) electric field, respectively. Additional details of the derivation of Eq. (1.9) is provided in the Appendix for interested readers. After applying the impedance boundary condition, the electromagnetic equation, Eq. (1.2), does not need to be solved within the plate and the coil. Nonetheless, the equation of heat diffusion, Eq. (1.6), is still solved within these two regions.

Based on the geometry of the specimens used in the experiment, the modeled sensitized HAZ is 3.2 mm (0.125 in) wide and located to either side of the weld (Fig. 5(b)). Recently, Tucker *et al.* [9] suggested that the formation of chromium carbide ($Cr_{23}C_6$) may lead to higher temperature in a sensitized region under induction heating, given that the electrical conductivity of $Cr_{23}C_6$ (7.87×10^5 S/m [35]) is lower than that of steels (1.69×10^6 S/m for the 440C specimen). Nonetheless, the detailed effects of variation in electrical conductivity on the IIRT result has not been shown. Moreover, the influence of other material parameters — particularly, magnetic permeability — is still unclear. To investigate the possible effects of electrical conductivity and magnetic permeability on the IIRT heat signature, we conduct a numerical parametric study in which either or both parameters are varied from their respective values for the unsensitized 440C steel.

4.4 Results and Discussion

4.4.1 Experimental results

Figure 6 shows the infrared (IR) images obtained from the IIRT experiment at 0.24 s, 0.34 s, 0.44 s, 0.56 s, 0.80 s, and 1.0 s after the induction wand is energized. The raw data obtained from the FLIR infrared camera (i.e. Analog to Digital (A/D) counts of intensity magnitude) is converted to temperature based on the Stefan-Boltzmann law and a reference image taken at a known temperature (75.5 °F). For ease of examination, dashed lines are added to the images afterwards to mark the weld location and the projected

location of the induction coil. Evidently, as time proceeds, the sensitized HAZ on either side of the weld exhibits a higher rate of temperature increase compared to both the region further away from the weld (that is, unaffected by the welding) and that of the weld line. Specifically, at 0.34 s, there is already a noticeable "hot zone" — that is, an area of disproportional temperature increase — seen to each side of the weld. The location of these "hot zones" coincides with the sensitized regions to either side of the weld. Between 0.34 s to 0.56 s, these two hot zones become more distinguishable, yet their sizes do not vary significantly. In other words, they clearly "mark" the two sensitized regions. This phenomenon can be explained by the fact that the thermal relaxation time derived from the heat equation (Eq. (1.6)),

$$t_{th} = d^2 \frac{\rho c_p}{4k}, \tag{1.11}$$

is approximately 0.6 s for the 440C steel and a characteristic length $d = 4$ mm. The last two images, taken at 0.80 s and 1.0 s, show that the regions of high temperature are beginning to expand due to thermal conduction.

For a closer examination of the IIRT result, Fig. 7 shows the spatial variation of temperature at 0.44 s along a 50.8 mm (2 in) line segment that is transverse to the weld, and passes through both the weld and the sensitized regions. The location of this line segment is marked in Fig. 6 (specifically, the image taken at 0.44 s) using a red dashed line. Despite some experimental noise due to the precision of the IR camera and imperfections in the surface of the specimen, two spikes can be clearly observed in the data, corresponding to geometric locations within the sensitized regions. Within these regions, the maximum temperature increase is found to be approximately 0.2 ˚F, which is 4 to 5 times higher than the temperature increase within the base material (i.e. 440C, unsensitized).

4.4.2 Numerical results

Figure 8 presents the temperature field at 0.44 s obtained from a representative IIRT simulation. In this simulation, the electrical conductivity (σ) and relative magnetic permeability (μ_r) are set to 2.94×10^5 S/m and 6000, respectively, within the sensitized HAZ regions. As expected, the region underneath the induction coil exhibits an increase of temperature due to induction heating, which is particularly noticeable within the HAZ regions.

For comparison with the experimental result, Fig. 9 shows the simulated temperature result along the same trackline used in the experiment. Clearly, the numerical simulation reproduces the same heat signature obtained from the IIRT experiment, which features two spikes marking the sensitized HAZ regions. The peak temperature obtained from the simulation is 77.65 ˚F, which is close to the experimental result (77.68 ˚F). The predicted temperature increase within the non-sensitized regions — namely the base 440C material and the weld line — also match reasonably well with their counterparts in the experiment. For example, the mean temperature between 25 mm and 15 mm from the center of the weld is predicted to be 77.55 ˚F, while the experimental result is 77.54 ˚F.

To investigate the cause of the disproportional heating within the sensitized HAZ regions, we have conducted a numerical parametric study in which the electrical conductivity (σ) within the HAZ is varied between 1.69×10^4 S/m and 8.47×10^6 S/m, and the relative magnetic permeability (μ_r) between 700 and 6000. Figure 10 presents the temperature result of four representative cases along the trackline mentioned above. Specifically,

(a) $\sigma = 1.69 \times 10^6$ S/m, $\mu_r = 700$;

(b) $\sigma = 1.69 \times 10^4$ S/m, $\mu_r = 700$;

(c) $\sigma = 1.69 \times 10^6$ S/m, $\mu_r = 6000$;

(d) $\sigma = 8.47 \times 10^5$ S/m, $\mu_r = 6000$.

In Case (a), both σ and μ_r in the HAZ are set to be the same as in the unsensitized base material (440C steel). This case is used as a baseline for comparisons. As expected, the temperature result along the trackline is nearly uniform, except for a small variation within the region of the weld, in which the material is set to be the 309 steel, i.e. the filler metal used in the experiment. Then, we reduce the value of σ while using the same μ_r. Case (b) is one example in which σ is reduced by a factor of 100. The result shows that while the IIRT result is indeed sensitive to the value of electrical conductivity σ, producing the heat signature observed in the experiment would require a 100-fold decrease of σ within the sensitized region, which is unlikely given the small volume fraction of the grain boundaries (cf. Fig. 3). This indicates that variation of σ may not be the only reason that allowed IIRT to detect the sensitized regions.

Next, we restore σ to its value in Case (a), and increase the value of μ_r in the HAZ. Case (c) is an example in which μ_r is increased to 6000, which is roughly the relative magnetic permeability of pure iron. This can be considered as a limiting case in which all the chromium and carbon atoms in the steel have been consumed to form chromium carbide[1]. The result presented in Fig. 10 shows that while increasing μ_r within the HAZ leads to a higher temperature therein, the magnitude of the temperature "spikes" observed in the IIRT experiment cannot be reproduced even in this limiting case. In other words, varying σ alone within the model will not accurately reproduce the magnitude of the IIRT temperature peaks within the sensitized HAZ to either side of the weld. Lastly, Case (d) is a representative case in which both σ and μ_r in the HAZ are varied, and the numerical result agrees reasonably well with the experimental data. This is also the case shown earlier in Figs. 8 and 9.

The numerical study suggests that the heat signature obtained from the IIRT experiment may result from an increase of both electrical resistivity and magnetic permeability within the sensitized regions. The increase of electrical resistivity can be related to the precipitation of chromium carbide near grain boundaries, as proposed by Tucker *et al.* [9]. In addition, we hypothesize that the increase of magnetic permeability in the sensitized HAZ may result from the loss of carbon and chromium atoms from the crystal lattice. Indeed, martensitic steels such as 440C possess an excess of carbon in their lattice structure through a rapid cooling process during manufacture, which traps these carbon atoms amongst the iron atoms. As sensitization takes this carbon out of the lattice to form $Cr_{23}C_6$, it is theorized that sensitized regions take on material properties closer to those of pure iron, which drives an increase in magnetic permeability.

Concluding Remarks: Welding-induced sensitization is a critical issue that affects the corrosion resistance of many alloys used in naval applications, including medium- and high-carbon stainless steels and aluminum alloys. In this project, we investigate the feasibility of using induction infrared thermography (IIRT) as a fast, non-destructive method for detecting welding-induced sensitization in stainless steels. A combined experimental and numerical research approach is employed, which includes SEM and IIRT experiments in a controlled laboratory environment and three-dimensional (3D) thermo-electro-magnetic simulations. Several key findings of this study are noteworthy. Firstly, the IIRT experiments show that a FLIR SC8203 infrared camera can clearly capture a distinguishable heat signature produced by welded 440C steel specimens after less than 1 second of inductive heating. The temperature increase within the sensitized region to either side of the weld line is found to be 4 to 5 times higher than that in the unsensitized base material. Secondly, using COMSOL Multiphysics, the proposed 3D thermo-electro-magnetic model is capable of simulating the IIRT experiment and reproducing the same heat signature. Specifically, the simulated temperature increase within the base material matches very closely the experimental result even for the very small (0.2 °F) induced temperature changes, which supports the validity of the numerical model. Moreover, the numerical parametric study suggests that the disproportional temperature increase within the sensitized regions may result from the increase of both electromagnetic permeability and electrical resistivity therein. The increase of electrical resistivity can be related to the production of chromium carbides, which is a characteristic phenomenon of sensitization in stainless steels. The increase of magnetic permeability may be related to the (possibly significant) loss of carbon and chromium atoms from the crystal lattice of the 440C steel.

A few limitations of this study and possible future directions should also be noted. The present study focuses

[1] In the 440C steel, the chromium/carbon molar ratio is approximately 22/6, which is very close to that in the $Cr_{23}C_6$ chromium carbide produced in the sensitization process.

on demonstrating IIRT for a specific steel, namely AISI 440C, and understanding the key physical mechanisms associated to this potential non-destructive evaluation method. The efficacy of IIRT for detecting sensitization in other steels, and possibly other alloys, requires additional investigation. Also, the IIRT setup employed in the present study is limited to detecting sensitization on the material's surface. Future studies may investigate the feasibility of IIRT for detecting sensitization underneath the surface of a structural component. Furthermore, additional laboratory experiments and simulations are needed to rigorously evaluate the hypotheses obtained from the numerical parametric studies.

4.5 Training and professional development

This project provided training and professional development opportunities for Mr. Matthew Roberts, who was a graduate student in the Department of Aerospace and Ocean Engineering and worked on this project as a graduate research assistant. Mr. Roberts participated in the design of research tasks, and conducted various theoretical, computational and experimental studies. In the summers of 2018 and 2019, he interned at NUWC Newport Division, where he conducted various laboratory experiments for this project using the facilities and equipment there. Mr. Roberts completed his MS Thesis on this project, and successfully defended it in 2019. He has presented his work at the 45th and 46th Annual Review of Progress in Quantitative Nondestructive Evaluation (QNDE), and at the ONR NURP annual program review meetings. After graduating from Virginia Tech in 2019, he joined NSWC Carderock Division.

Emily Guzas and Kevin Wang, together with other colleagues, established an Educational Partnership between NUWC-Newport and Virginia Tech. The Partnership Agreement has been signed off by Commanding Officer of NUWC-Newport, Michael R. Coughlin, and Assistant Vice President of Virginia Tech, Linda R. Bucy.

4.6 Dissemination of results

- M. Roberts, Induction Infrared Thermography for Non-Destructive Evaluation of Alloy Sensitization, M.S. Thesis, Virginia Tech, 2019 (Thesis)
- M. Roberts, K. Wang, E. Guzas, W. Tucker, P. Lockhart, Induction Infrared Thermography for Non-Destructive Evaluation of Welding-Induced Sensitization in Stainless Steels, *Journal of Nondestructive Evaluation*, under review (Journal paper)
- W. Tucker, P. Lockhart, E. Guzas, Evaluating Sensitized Chromium Steel Alloys with Induction Infrared Thermography, *Journal of Nondestructive Evaluation* 38(2), 2019 (Journal paper)
- E. Guzas, M. Roberts, K. Wang, Induction Infrared Thermography for Non-Destructive Evaluation of Alloy Sensitization, *Proceedings of the 45th Annual Review of Progress in Quantitative Nondestructive Evaluation (QNDE 2018).* Burlington, VT, 2018 (Conference paper and presentation)
- M. Roberts, K. Wang, E. Guzas, Induction Infrared Thermography for Non-Destructive Evaluation of Alloy Sensitization, the 46th Annual Review of Progress in Quantitative Nondestructive Evaluation (QNDE 2019). Portland, OR, 2019 (Conference presentation)

4.7 Honors

Matthew Roberts has been awarded an internship provided by ONR's Naval Research Enterprise Intern Program (NREIP) for the summers of 2018 and 2019.

5 Technology Transfer

Throughout the performance period, Matthew Roberts and Kevin Wang worked closely with researchers at NUWC Newport Division, including Emily Guzas, Wayne Tucker and Patric Lockhart.

6 Participants

- Kevin Wang, PI, one month per year for two years.
- Matthew Roberts, Graduate Research Assistant, twelve months per year for two years.
- Emily Guzas, Navy Mentor, funded through a separate contract between ONR and NUWC Newport Division.

7 Products

- M. Roberts, Induction Infrared Thermography for Non-Destructive Evaluation of Alloy Sensitization, M.S. Thesis, Virginia Tech, 2019 (Thesis)
- M. Roberts, K. Wang, E. Guzas, W. Tucker, P. Lockhart, Induction Infrared Thermography for Non-Destructive Evaluation of Welding-Induced Sensitization in Stainless Steels, *Journal of Nondestructive Evaluation*, under review (Journal paper)
- W. Tucker, P. Lockhart, E. Guzas, Evaluating Sensitized Chromium Steel Alloys with Induction Infrared Thermography, *Journal of Nondestructive Evaluation* 38(2), 2019 (Journal paper)
- E. Guzas, M. Roberts, K. Wang, Induction Infrared Thermography for Non-Destructive Evaluation of Alloy Sensitization, *Proceedings of the 45th Annual Review of Progress in Quantitative Nondestructive Evaluation (QNDE 2018).* Burlington, VT, 2018 (Conference paper and presentation)
- M. Roberts, K. Wang, E. Guzas, Induction Infrared Thermography for Non-Destructive Evaluation of Alloy Sensitization, the 46th Annual Review of Progress in Quantitative Nondestructive Evaluation (QNDE 2019). Portland, OR, 2019 (Conference presentation)

All the above research products have been approved for public release: distribution unlimited (DISTRIBUTION A).

Appendix: Additional details on the governing electromagnetic equation and the impedance boundary condition

One of the primary governing equations comes in the form of the magnetic vector potential formulation of the electromagnetic diffusion equation derived from Maxwell's equations.

$$i\omega\sigma\mathbf{A} - \frac{1}{\mu}\nabla^2\mathbf{A} = \mathbf{J}_s. \tag{1.12}$$

To arrive at this result, the following derivation is undertaken.

From Maxwell's Law of Induction, the curl of an electric field ($\mathbf{E}$) is equal to the negative time derivative of the magnetic field ($\mathbf{B}$), i.e.

$$\nabla \times \mathbf{E} = -\frac{\partial \mathbf{B}}{\partial t}. \tag{1.13}$$

From Gauss's Law for Magnetism,

$$\nabla \cdot \mathbf{B} = 0. \tag{1.14}$$

Therefore, the magnetic field $\mathbf{B}$ can be written in terms of $\mathbf{A}$, the magnetic vector potential:

$$\mathbf{B} = \nabla \times \mathbf{A}. \tag{1.15}$$

Substituting (1.15) into (1.13) yields

$$\nabla \times \mathbf{E} = -\frac{\partial}{\partial t}\big(\nabla \times \mathbf{A}\big) = -\nabla \times \frac{\partial \mathbf{A}}{\partial t}, \tag{1.16}$$

or equivalently,

$$\nabla \times \left(\mathbf{E} + \frac{\partial \mathbf{A}}{\partial t}\right) = 0. \tag{1.17}$$

Because the curl of a gradient of a vector field is 0, one possible solution to (1.17) is given by

$$\mathbf{E} = -\frac{\partial \mathbf{A}}{\partial t} - \nabla\varphi, \tag{1.18}$$

where φ is the electric scalar potential. This expression can be interpreted as a combination of an induced electric field ($\mathbf{E}_i$) and an applied (i.e. source) electric field ($\mathbf{E}_s$), i.e.

$$\mathbf{E} = -\frac{\partial \mathbf{A}}{\partial t} - \nabla\varphi = \mathbf{E}_i + \mathbf{E}_s. \tag{1.19}$$

Multiplying the electric field by the electrical conductivity (σ), the result relates current density ($\mathbf{J}$) to the magnetic vector potential (the continuum form of Ohm's law):

$$\mathbf{J} = \sigma\mathbf{E} = -\sigma\frac{\partial \mathbf{A}}{\partial t} - \sigma\nabla\varphi = -\sigma\frac{\partial \mathbf{A}}{\partial t} + \mathbf{J}_s. \tag{1.20}$$

By Ampere's law,

$$\mathbf{J} = \nabla \times \frac{1}{\mu}\mathbf{B}, \tag{1.21}$$

where μ denotes the material's magnetic permeability, assumed here to be a constant. Combining Equations (1.15), (1.20), and (1.21), we obtain

$$\frac{1}{\mu}\nabla \times \nabla \times \mathbf{A} = -\sigma\frac{\partial \mathbf{A}}{\partial t} + \mathbf{J}_s. \tag{1.22}$$

Through a vector identity, (1.22) can be re-written as

$$\frac{1}{\mu}\Big(\nabla(\nabla\cdot\mathbf{A})-\nabla^2\mathbf{A}\Big)=-\sigma\frac{\partial\mathbf{A}}{\partial t}+\mathbf{J}_s. \tag{1.23}$$

By imposing the Coulomb gauge condition,

$$\nabla\cdot\mathbf{A}=0, \tag{1.24}$$

we arrive at the final form of the diffusion equation in the time domain,

$$-\frac{1}{\mu}\nabla^2\mathbf{A}=-\sigma\frac{\partial\mathbf{A}}{\partial t}+\mathbf{J}_s. \tag{1.25}$$

Assuming $\mathbf{J}_s$ and $\mathbf{A}$ are harmonic, the above equation can be moved from the time domain to the frequency domain through a phase transformation, i.e.

$$\mathbf{J}_s=\mathbf{J}_{s0}e^{i\omega t},\qquad \mathbf{A}=\mathbf{A}_0e^{i\omega t}. \tag{1.26}$$

Employing (1.26) into (1.25), and dropping the subscript "0", we obtain

$$i\omega\sigma\mathbf{A}-\frac{1}{\mu}\nabla^2\mathbf{A}=\mathbf{J}_s. \tag{1.27}$$

The final magnetic vector potential, $\mathbf{A}$, is found by solving this diffusion equation in the frequency domain. Upon finding the solution for the magnetic vector potential, the eddy currents in the plate are described by

$$\mathbf{J}=-i\omega\sigma\mathbf{A}. \tag{1.28}$$

At a surface with impedance η, the electric field ($\mathbf{E}$) and the magnetic field ($\mathbf{H}$) are related through

$$\mathbf{n}\times(\mathbf{n}\times\mathbf{E})=-\eta\mathbf{n}\times\mathbf{H}, \tag{1.29}$$

where $\mathbf{n}$ denotes the unit surface normal. For example, for a planar surface in the x-y plane, Eq. (1.29) gives

$$E_x=-\eta H_y \tag{1.30}$$

$$E_y=\eta H_x. \tag{1.31}$$

Again, the electric field $\mathbf{E}$ can be written as the combination of an induced field and an applied source field, i.e.

$$\mathbf{E}=\mathbf{E}_i+\mathbf{E}_s. \tag{1.32}$$

Substituting (1.32) into (1.29) yields

$$\mathbf{n}\times(\mathbf{n}\times\mathbf{E}_i)+\mathbf{n}\times(\mathbf{n}\times\mathbf{E}_s)=-\eta\mathbf{n}\times\mathbf{H}. \tag{1.33}$$

Applying vector identity

$$\mathbf{a}\times(\mathbf{b}\times\mathbf{c})=(\mathbf{a}\cdot\mathbf{c})\mathbf{b}-(\mathbf{a}\cdot\mathbf{b})\mathbf{c},\qquad\forall\mathbf{a},\mathbf{b},\mathbf{c}, \tag{1.34}$$

Equation (1.33) becomes

$$(\mathbf{n}\cdot\mathbf{E}_i)\mathbf{n}-\mathbf{E}_i+(\mathbf{n}\cdot\mathbf{E}_s)\mathbf{n}-\mathbf{E}_s=-\eta\mathbf{n}\times\mathbf{H}. \tag{1.35}$$

Therefore, with surface impedance ([34])

$$\eta=-\sqrt{\frac{\mu}{\varepsilon-\frac{i\sigma}{\omega}}}, \tag{1.36}$$

we obtain the impedance boundary condition adopted in the COMSOL simulations, i.e.

$$\sqrt{\frac{\mu}{\varepsilon-\frac{i\sigma}{\omega}}}\mathbf{n}\times\mathbf{H}+\mathbf{E}_i-(\mathbf{n}\cdot\mathbf{E}_i)\mathbf{n}=(\mathbf{n}\cdot\mathbf{E}_s)\mathbf{n}-\mathbf{E}_s. \tag{1.37}$$

References

[1] Denny A Jones. *Principles and prevention of corrosion. 2*. Prentice Hall, 1996.

[2] Emily C Cormack. The effect of sensitization on the stress corrosion cracking of aluminum alloy 5456. Technical report, Naval Postgraduate School, Monterey, CA, 2012.

[3] Ronald L Holtz, Peter S Pao, Robert A Bayles, Thomas M Longazel, and Ramasis Goswami. Corrosion-fatigue behavior of aluminum alloy 5083-h131 sensitized at 448 k (175 c). *Metallurgical and Materials Transactions A*, 43(8):2839–2849, 2012.

[4] Jinlong Lv, Tongxiang Liang, Limin Dong, and Chen Wang. Influence of sensitization on microstructure and passive property of aisi 2205 duplex stainless steel. *Corrosion Science*, 104:144–151, 2016.

[5] RC Scarberry, SC Pearman, and JR Crum. Precipitation reactions in inconel alloy 600 and their effect on corrosion behavior. *Corrosion*, 32(10):401–406, 1976.

[6] Gary S Was and RM Kruger. A thermodynamic and kinetic basis for understanding chromium depletion in ni-cr-fe alloys. *Acta metallurgica*, 33(5):841–854, 1985.

[7] John C Lippold and Damian J Kotecki. *Welding metallurgy and weldability of stainless steels*. Wiley, 2005.

[8] TM Devine. The mechanism of sensitization of austenitic stainless steel. *Corrosion science*, 30(2-3):135–151, 1990.

[9] Wayne C Tucker, Patric Lockhart, and Emily Guzas. Evaluating sensitized chromium steel alloys with induction infrared thermography. *Journal of Nondestructive Evaluation*, 38(2):42, 2019.

[10] ASTM A262-15: Standard practices for detecting susceptibility to intergranular attack in austenitic stainless steels. Standard, ASTM International, West Conshocken, PA, 2015.

[11] ASTM G67-18: Standard test method for determining the susceptibility to intergranular corrosion of 5XXX series aluminum alloys by mass loss after exposure to nitric acid (NAMLT test). Standard, ASTM International, West Conshocken, PA, 2018.

[12] JM Aquino, CA Della Rovere, and SE Kuri. Intergranular corrosion susceptibility in supermartensitic stainless steel weldments. *Corrosion Science*, 51(10):2316–2323, 2009.

[13] C Garcia, MP De Tiedra, Y Blanco, O Martin, and F Martin. Intergranular corrosion of welded joints of austenitic stainless steels studied by using an electrochemical minicell. *Corrosion Science*, 50(8):2390–2397, 2008.

[14] AISI G108-94 (2015): Standard Test Method for Electrochemical Reactivation (EPR) for Detecting Sensitization of AISI Type 304 and 304L Stainless Steels. Standard, ASTM International, West Conshocken, PA, 2015.

[15] Bo Deng, Yiming Jiang, Juliang Xu, Tao Sun, Juan Gao, Lihua Zhang, Wei Zhang, and Jin Li. Application of the modified electrochemical potentiodynamic reactivation method to detect susceptibility to intergranular corrosion of a newly developed lean duplex stainless steel ldx2101. *Corrosion Science*, 52(3):969–977, 2010.

[16] Vivekanand Kain, RC Prasad, and PK De. Testing sensitization and predicting susceptibility to intergranular corrosion and intergranular stress corrosion cracking in austenitic stainless steels. *Corrosion*, 58(1):15–37, 2002.

[17] Hasan Shaikh, N Sivaibharasi, B Sasi, T Anita, R Amirthalingam, BPC Rao, T Jayakumar, HS Khatak, and Baldev Raj. Use of eddy current testing method in detection and evaluation of sensitisation and intergranular corrosion in austenitic stainless steels. *Corrosion Science*, 48(6):1462–1482, 2006.

[18] Hiroaki Kikuchi, Hiroki Yanagiwara, Hideki Takahashi, Takaki Sumimoto, and Takeshi Murakami. Detection of sensitization for 600 alloy and austenitic stainless steel by magnetic field sensor. In *19th World Conference on Non-Destructive Testing, Munich, Germany*, 2016.

[19] Saju T Abraham, SK Albert, CR Das, N Parvathavarthini, B Venkatraman, RS Mini, and K Balasubramaniam. Assessment of sensitization in aisi 304 stainless steel by nonlinear ultrasonic method. *Acta Metallurgica Sinica (English Letters)*, 26(5):545–552, 2013.

[20] Adam Cobb, Erica Macha, Jonathan Bartlett, and Yanquan Xia. Detecting sensitization in aluminum alloys using acoustic resonance and emat ultrasound. In *AIP Conference Proceedings*, volume 1806, page 050001. AIP Publishing, 2017.

[21] J Stella, J Cerezo, and E Rodriguez. Characterization of the sensitization degree in the aisi 304 stainless steel using spectral analysis and conventional ultrasonic techniques. *NDT & E International*, 42(4):267–274, 2009.

[22] G Zenzinger, J Bamberg, W Satzger, and V Carl. Thermographic crack detection by eddy current excitation. *Nondestructive Testing and Evaluation*, 22(2-3):101–111, 2007.

[23] Ilham Zainal Abidin, Gui Yun Tian, John Wilson, Suixian Yang, and Darryl Almond. Quantitative evaluation of angular defects by pulsed eddy current thermography. *Ndt & E International*, 43(7):537–546, 2010.

[24] Liang Cheng and Gui Yun Tian. Surface crack detection for carbon fiber reinforced plastic (cfrp) materials using pulsed eddy current thermography. *IEEE Sensors Journal*, 11(12):3261–3268, 2011.

[25] NS Rusli, IZ Abidin, and SA Aziz. A review on eddy current thermography technique for non-destructive testing application. *Jurnal Teknologi*, 78(11), 2016.

[26] Beate Oswald-Tranta. Induction thermography for surface crack detection and depth determination. *Applied Sciences*, 8(2):257, 2018.

[27] Martin Fisk. *Simulation of induction heating in manufacturing*. PhD thesis, Luleå tekniska universitet, 2008.

[28] B Oswald-Tranta. Thermo-inductive crack detection. *Nondestructive Testing and Evaluation*, 22(2-3):137–153, 2007.

[29] COMSOL Inc. *COMSOL Multiphysics 5.3a*. COMSOL Inc., Stockholm, Sweden, 2017.

[30] ASTM E3-11(2017): Standard Guide for Preparation of Metallographic Specimens. Standard, ASTM International, West Conshocken, PA, 2017.

[31] ASTM A763-15: Standard Practices for Detecting Susceptibility to Intergranular Attack in Ferritic Stainless Steels. Standard, ASTM International, West Conshocken, PA, 2015.

[32] Subhas Chandra Mukhopadhyay. *New developments in sensing technology for structural health monitoring*, volume 96. Springer, 2011.

[33] TBA Senior. Impedance boundary conditions for imperfectly conducting surfaces. *Applied Scientific Research, Section B*, 8(1):418, 1960.

[34] COMSOL Inc. Technical Staff. Ac/dc module 5.3a user's guide. Technical report, COMSOL Inc., 2017.

[35] SN L'vov, VF Nemchenko, PS Kislyi, TS Verkhoglyadova, and T Ya Kosolapova. The electrical properties of chromium borides, carbides, and nitrides. *Soviet Powder Metallurgy and Metal Ceramics*, 1(4):243–247, 1962.

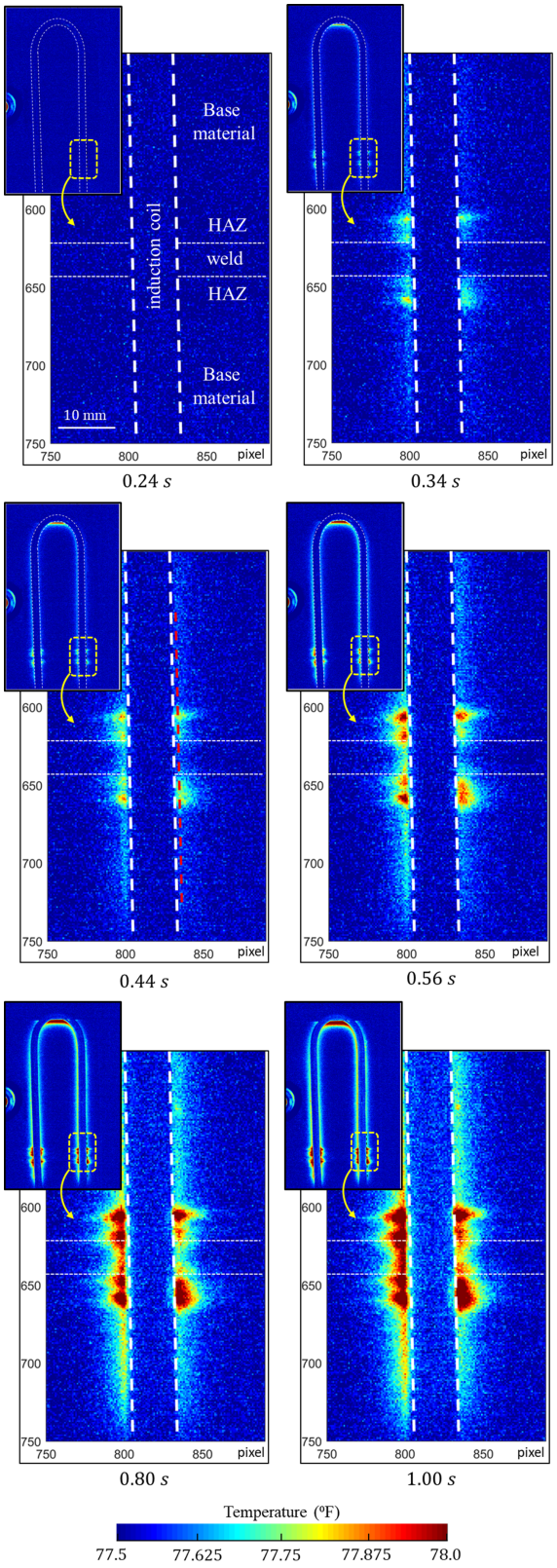

Figure 6: Result of IIRT Experiment: Variation of temperature in time, up to 1 s. (Temperature in the region of the plate underneath the induction coil is not captured, due to the obstruction of the coil.)

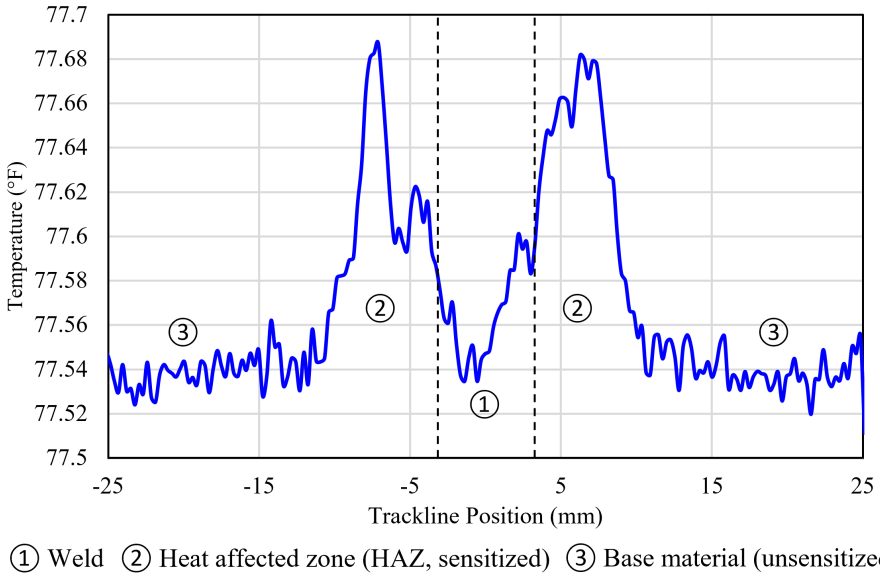

Figure 7: Result of IIRT Experiment: Temperature along trackline at $t = 0.44$ s. (The location of the trackline is marked in Fig. 6 as a red dashed line.)

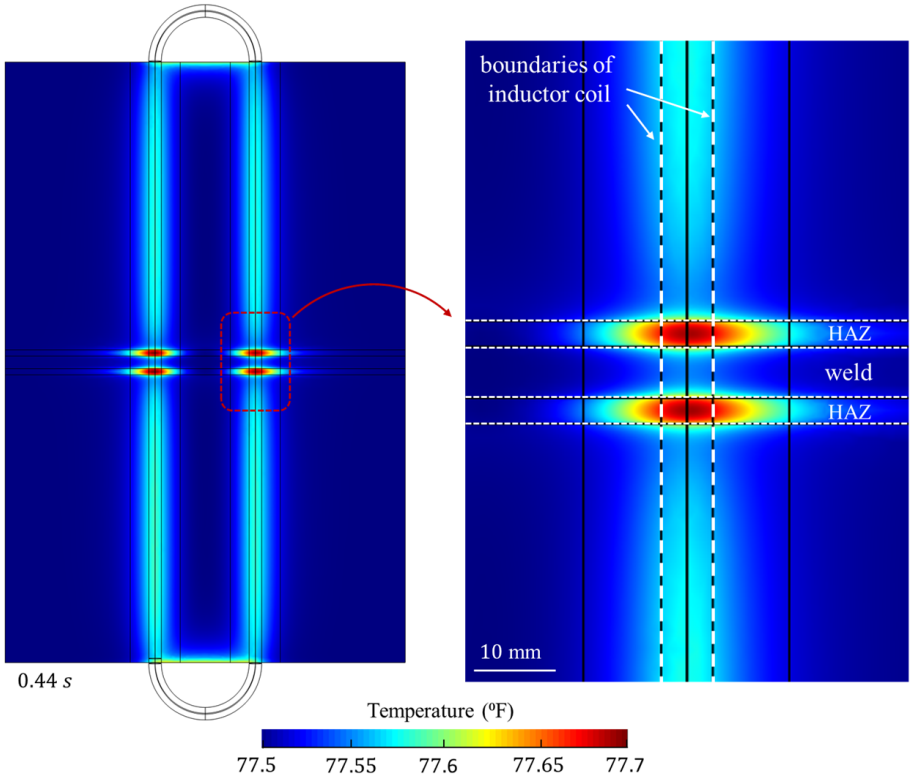

Figure 8: Result of IIRT simulation: Temperature field at 0.44 s.

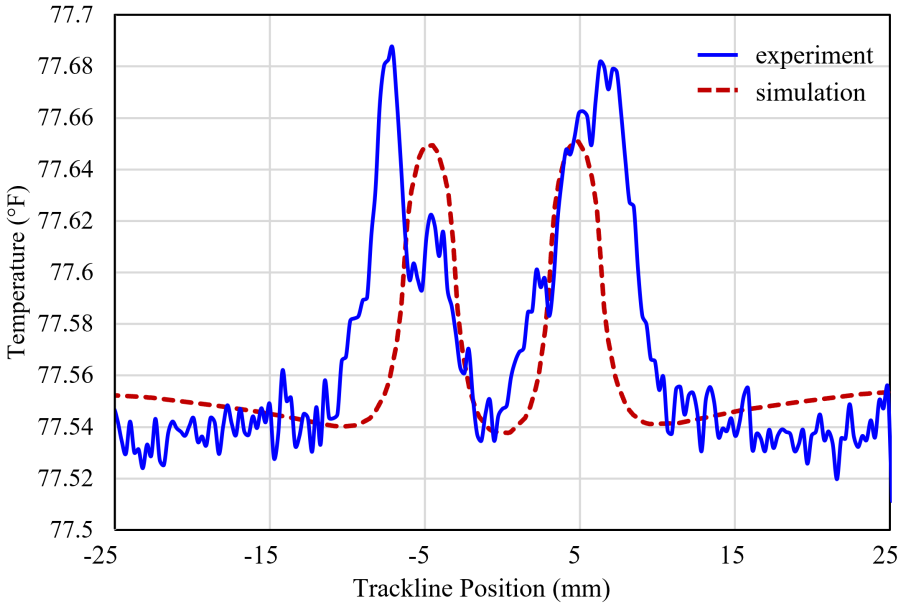

Figure 9: Result of IIRT simulation: Temperature along trackline at 0.44 s.

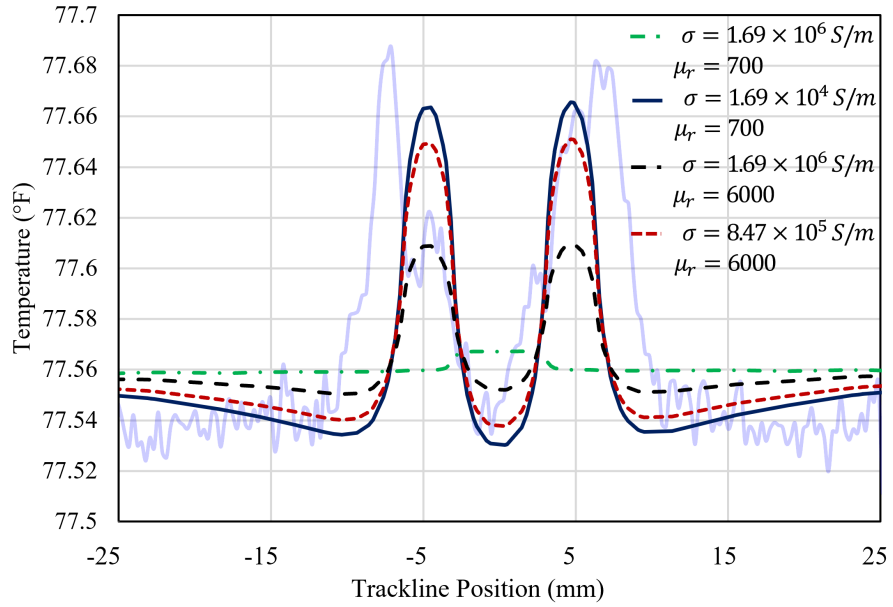

Figure 10: Comparison of IIRT simulations with different values of electrical conductivity (σ) and relative magnetic permeability (μ_r) in the HAZ regions: Temperature along a trackline at 0.44 s. (The experimental result is plotted as a transparent curve in the background.